

1 **The effects of different footprint sizes and cloud algorithms on the**
2 **top-of-atmosphere radiative flux calculation from the Clouds and**
3 **Earth's Radiant Energy System (CERES) instrument on**
4 **Suomi-NPP**

5 WENYING SU, *

Science Directorate, NASA Langley Research Center, Hampton, Virginia

6 LUSHENG LIANG, WALTER F. MILLER, VICTOR E. SOTHCOTT

Science Systems & Applications, Inc., Hampton, Virginia

* *Corresponding author address:* Wenying Su, MS420, NASA Langley Research Center, Hampton, VA 23681.

E-mail: Wenying.Su-1@nasa.gov

ABSTRACT

7
8 Only one CERES instrument is onboard the Suomi-NPP and it has been placed in cross-track
9 mode since launch, it is thus not possible to construct a set of angular distribution models
10 (ADMs) specific for CERES on NPP. Edition 4 Aqua ADMs are used for flux inversions for
11 CERES-NPP measurements. However, the footprint size of CERES-NPP is greater than
12 that of CERES-Aqua, as the altitude of the NPP orbit is higher than that of the Aqua orbit.
13 Furthermore, cloud retrievals from the Visible Infrared Imaging Radiometer Suite (VIIRS)
14 and the Moderate Resolution Imaging Spectroradiometer (MODIS), the imagers sharing the
15 spacecrafts with CERES-NPP and CERES-Aqua, are also different. To quantify the flux
16 uncertainties due to the footprint size difference between CERES-Aqua and CERES-NPP,
17 and due to both the footprint size difference and cloud property difference, a simulation
18 is designed using the MODIS pixel level data which are convolved with the CERES-Aqua
19 and CERES-NPP point spread functions into their respective footprints. The simulation is
20 designed to isolate the effects of footprint size and cloud property differences on flux uncer-
21 tainty from calibration and orbital differences between CERES-NPP and CERES-Aqua. The
22 footprint size difference between CERES-Aqua and CERES-NPP introduces instantaneous
23 flux uncertainties in monthly gridded CERES-NPP of less than 4.0 Wm^{-2} for SW, and less
24 than 1.0 Wm^{-2} for both daytime and nighttime LW. The global monthly mean instantane-
25 ous SW flux from simulated CERES-NPP has a low bias of 0.4 Wm^{-2} when compares
26 to simulated CERES-Aqua, and the root-mean-square (RMS) error is 2.2 Wm^{-2} between
27 them; the biases of daytime and nighttime LW flux are close to zero with RMS errors of 0.8
28 Wm^{-2} and 0.2 Wm^{-2} . These uncertainties are within the uncertainties of CERES ADMs.
29 When both footprint size and cloud property (cloud fraction and optical depth) differences
30 are considered, the uncertainties of monthly gridded CERES-NPP SW flux can be up to
31 20 Wm^{-2} in the Arctic regions where cloud optical depth retrievals from VIIRS differ sig-
32 nificantly from MODIS. The global monthly mean instantaneous SW flux from simulated
33 CERES-NPP has a high bias of 1.1 Wm^{-2} and the RMS error increases to 5.2 Wm^{-2} . LW

34 flux shows less sensitivity to cloud property differences than SW flux, with the uncertainties
35 of about 2 Wm^{-2} in monthly gridded LW flux, and the RMS errors of global monthly mean
36 daytime and nighttime fluxes increase only slightly. These results highlight the importance
37 of consistent cloud retrieval algorithms to maintain the accuracy and stability of the CERES
38 climate data record.

1. Introduction

The Clouds and Earth’s Radiant Energy System (CERES) project has been providing data products critical to advancing our understanding of the effects of clouds and aerosols on radiative energy within the Earth-atmosphere system. CERES data are used by the science community to study the Earth’s energy balance (e.g., Trenberth et al. 2009; Kato et al. 2011; Loeb et al. 2012; Stephens et al. 2012), aerosol direct radiative effects (e.g., Satheesh and Ramanathan 2000; Zhang et al. 2005; Loeb and Manalo-Smith 2005; Su et al. 2013), aerosol-cloud interactions (e.g., Loeb and Schuster 2008; Quaas et al. 2008; Su et al. 2010b), and to evaluate global general circulation models (e.g., Pincus et al. 2008; Su et al. 2010a; Wang and Su 2013; Wild et al. 2013).

Six CERES instruments have flown on four different satellites thus far. CERES pre-Flight Model (FM) on Tropical Rainfall Measuring Mission (TRMM) was launched on November 27, 1997 into a 350-km circular precessing orbit with a 35° inclination angle and flew together with the Visible and Infrared Scanner (VIRS). CERES instruments (FM1 and FM2) on Terra were launched on December 18, 1999 into a 705-km sun-synchronous orbit with a 10:30 a.m. equatorial crossing time. CERES instruments (FM3 and FM4) on Aqua satellite were launched on May 4, 2002 into a 705-km sun-synchronous orbit with a 1:30 p.m. equatorial crossing time. CERES on Terra and Aqua flies alongside Moderate-Resolution Imaging Spectroradiometer (MODIS). CERES instrument (FM5) was launched onboard Suomi-NPP (hereafter referred to as NPP) on October 28, 2011 into a 824-km sun-synchronous orbit with a 1:30 p.m. equatorial crossing time and flies alongside the Visible Infrared Imaging Radiometer Suite (VIIRS). As the orbit altitudes differ among these satellites, the spatial resolutions of CERES instruments also vary from each other. TRMM has the lowest orbit altitude and offers the highest spatial resolution of CERES measurements, about 10 km at nadir; the spatial resolution of CERES on Terra and Aqua is about 20 km at nadir; and is about 24 km at nadir for NPP as it has the highest orbit altitude.

The CERES instrument consists of a three-channel broadband scanning radiometer (Wielicki

66 et al. 1996). The scanning radiometer measures radiances in shortwave (SW, 0.3-5 μm), win-
 67 dow (WN, 8-12 μm), and total (0.3-200 μm) channels. The longwave (LW) component is
 68 derived as the difference between total and SW channels. These measured radiances (I) at
 69 a given sun-Earth-satellite geometry are converted to outgoing reflected solar and emitted
 70 thermal TOA radiative fluxes (F) as:

$$F(\theta_0) = \frac{\pi I(\theta_0, \theta, \phi)}{R_j(\theta_0, \theta, \phi)}. \quad (1)$$

71 where θ_0 is the solar zenith angle, θ is the CERES viewing zenith angle, ϕ is the relative
 72 azimuth angle between CERES and the solar plane, and $R_j(\theta_0, \theta, \phi)$ is the anisotropic factors
 73 for scene type j . Here scene type is a combination of variables (e.g., surface type, cloud
 74 fraction, cloud optical depth, cloud phase, aerosol optical depth, precipitable water, lapse
 75 rate, etc) that are used to group the data to develop distinct angular distribution models
 76 (ADMs). Note the SW ADMs are developed as a function of θ_0, θ, ϕ for each scene type,
 77 whereas the LW ADMs are a weak function of θ_0 and ϕ and are developed only as a function
 78 of θ (Loeb et al. 2005; Su et al. 2015a).

79 To facilitate the construction of ADMs, there are pairs of identical CERES instruments
 80 on both Terra and Aqua. At the beginning of these missions one of the instruments on each
 81 satellite was always placed in a rotating azimuth plane (RAP) scan mode, while the other
 82 one was placed in cross-track mode to provide spatial coverage. When in RAP mode, the
 83 instrument scans in elevation as it rotates in azimuth, thus acquiring radiance measurements
 84 from a wide range of viewing combinations. There are about 60 months of RAP data collected
 85 on Terra and about 32 months of RAP data collected on Aqua. CERES instruments fly
 86 alongside high-resolution imagers, which provide accurate scene type information within
 87 the CERES footprints. Cloud and aerosol retrievals based upon high-resolution imager
 88 measurements are averaged over the CERES footprints by accounting for the CERES point
 89 spread function (PSF, Smith 1994) and are used for scene type classification. Similarly,
 90 spectral radiances from MODIS/VIIRS observations are averaged over the CERES footprints
 91 weighted by the CERES PSF. Surface types are obtained from the International Geosphere

92 Biosphere Program (IGBP, Loveland and Belward 1997) global land cover data set. Fresh
93 snow and sea ice surface types are derived from a combination of the National Snow and Ice
94 Data Center (NSIDC) microwave snow/ice map and the National Environmental Satellite,
95 Data and Information Service (NESDIS) snow/ice map. NESDIS uses imager data to identify
96 snow and sea ice and provide snow and sea ice information near the coast, whereas NSIDC
97 does not provide microwave retrievals within 50 km of the coast.

98 TRMM ADMs were developed using 9 months of CERES observations and the scene
99 identification information retrieved from VIRS observations (Loeb et al. 2003). Terra ADMs
100 and Aqua ADMs were developed separately using multi-year CERES Terra and Aqua mea-
101 surements in RAP mode and in cross-track mode using the scene identification information
102 from Terra MODIS and Aqua MODIS (Loeb et al. 2005; Su et al. 2015a). The high-resolution
103 MODIS imager provides cloud conditions for every CERES footprint. The cloud algorithms
104 developed by the CERES cloud working group retrieve cloud fraction, cloud optical depth,
105 cloud phase, cloud top and effective temperature/pressure (among other variables) based on
106 MODIS pixel-level measurements (Minnis et al. 2010). These pixel-level cloud properties
107 are spatially and temporally matched with the CERES footprints and are used to select the
108 scene-dependent ADMs to convert the CERES measured radiances to fluxes (Eq.1). The
109 spatial matching criterion used is 1 km. The temporal matching criterion used is less than
110 20 seconds when CERES is in cross-track mode, and less than 6 minutes when CERES is in
111 RAP mode.

112 There is only one CERES instrument on NPP and it has been placed in cross-track scan
113 mode since launch, it is thus not feasible to develop a specific set of ADMs for CERES
114 on NPP. Currently, the Edition 4 Aqua ADMs (Su et al. 2015a) are used to invert fluxes
115 for the CERES measurements on NPP. The CERES footprint size on NPP is larger than
116 that on Aqua. As pointed out by Di Girolamo et al. (1998), the nonreciprocal behavior
117 of the radiation field depends on measurement resolution, which means the ADMs do too.
118 They concluded that ADMs should be applied only to data of the same resolution as the

119 data used to derive the ADMs. Since the footprint sizes are different between CERES-Aqua
120 and CERES-NPP, will using ADMs developed based upon CERES-Aqua measurements for
121 CERES-NPP flux inversion introduce any uncertainties in the CERES-NPP flux? Addition-
122 ally, ADMs are scene type dependent, it is important to use consistent scene identification
123 for developing and applying the ADMs. However, the VIIRS channels are not identical to
124 those of MODIS, especially the lack of $6.7 \mu\text{m}$ and $13.3 \mu\text{m}$ channels, caused the cloud prop-
125 erties retrieved from MODIS and VIIRS differ from each other. These differences affect the
126 scene identification used to select the ADMs for flux inversion and thus can lead to addi-
127 tional uncertainties in the CERES-NPP flux. In this study, we design a simulation study to
128 quantify the CERES-NPP flux uncertainties due to the footprint size difference alone, and
129 due to both the footprint size and cloud property differences.

130 **2. Comparison between CERES-Aqua and CERES-NPP**

131 Besides the altitude differences between Aqua and NPP satellites, they are also different
132 in other orbital characteristics. For example, the orbital period for Aqua is about 98.82
133 minutes, while it is about 101.44 minutes for NPP; and the orbital inclination for Aqua is
134 about 98.20° , while it is about 98.75° for NPP. These orbital differences result in different
135 local overpass times between Aqua and NPP and their orbits fly over each other about every
136 64 hours. These simultaneous observations from Aqua and NPP are matched to compare
137 SW and LW radiances using CERES Aqua Edition 4 Single Scanner Footprint TOA/Surface
138 Fluxes and Clouds (SSF) product and CERES NPP Edition 1 SSF product. Here we use I_a^m
139 to denote the CERES-Aqua (subscript a) measured (superscript m) radiance, and I_n^m as the
140 CERES-NPP (subscript n) measured radiance. Similarly, F_a^m and F_n^m are the fluxes derived
141 from I_a^m and I_n^m using CERES Aqua ADMs. The matching criteria used for SW radiances
142 are that the latitude and longitude differences between the Aqua footprints and the NPP
143 footprints are less than 0.05 degree, solar zenith angle and viewing zenith angle differences

144 are less than 2 degrees, and relative azimuth angle difference is less than 5 degrees. The
145 matching criteria used here also provide a tight constraint on scattering angles, with about
146 95.6% and 99.9% of the matched footprints having scattering angle differences less than
147 2 degrees and 3 degrees. Same latitude and longitude matching criteria are used for LW
148 radiances and the viewing zenith angle difference between the Aqua footprints and the NPP
149 footprints is less than 2 degrees.

150 Figure 1 shows the SW, daytime LW, and nighttime LW radiance comparisons between
151 CERES-Aqua and CERES-NPP using matched footprints of 2013 and 2014. The total
152 number of matched footprints, the mean I_a^m and I_n^m , and the root-mean-square (RMS) errors
153 are summarized in Table 1. The mean SW I_n^m is about $1 \text{ Wm}^{-2}\text{sr}^{-1}$ greater than I_a^m , the mean
154 daytime LW I_n^m is about $0.4 \text{ Wm}^{-2}\text{sr}^{-1}$ smaller than I_a^m , and the nighttime LW I_n^m and I_a^m
155 agree to within $0.1 \text{ Wm}^{-2}\text{sr}^{-1}$. Excluding matched footprints with scattering angle difference
156 greater than 2 degrees does not change the SW comparison result. These comparisons
157 include data taken from nadir to oblique viewing angles ($\theta > 60$). The RMS errors remain
158 almost the same when we compare the radiances taken at different θ ranges. Footprint size
159 differences may also contribute to the radiance differences, but these radiance differences
160 should be random. It is likely that the footprint size differences can increase the RMS errors,
161 but the mean radiance differences are mostly resulted from calibration differences between
162 CERES-Aqua and CERES-NPP. As mentioned earlier, the daytime CERES LW radiance
163 is derived as the difference between total channel and SW channel measurements, and the
164 nighttime CERES LW radiance is directly derived from the total channel measurements.
165 The differences shown in Table 1 indicate that the agreement of the total channels between
166 CERES-Aqua and CERES-NPP are better than that of the SW channels, leading to a smaller
167 daytime LW difference than SW difference. Loeb et al. (2016) examined the normalized
168 instrument gains for the total and SW channels for CERES FM1-FM5 since the beginning
169 of the mission (BOM). The total channel response to LW radiation has gradually increased
170 with time for all instruments. For the two instruments (FM3 and FM5) that are of interest

171 here, the increases relative to the BOM are 0.7% for FM3 and 0.4% for FM5. The SW
 172 channel response increases about 0.4% for FM3 and decreases by 0.2% for FM5. Exact
 173 causes for the calibration differences between CERES-Aqua and CERES-NPP are not yet
 174 known and more research are needed to understand their differences. The future plan is to
 175 place CERES-NPP on the same radiometric scale as CERES-Aqua.

176 Flux comparison using the same matched footprints are shown in Figure 2 and the mean
 177 F_a^m and F_n^m , and the RMS errors between them are summarized in Table 1. Consistent with
 178 the radiance comparisons, the mean SW F_n^m is about 3.8 Wm^{-2} greater than F_a^m , the mean
 179 daytime LW F_n^m is about 1.0 Wm^{-2} smaller than F_a^m , and the mean nighttime LW F_n^m is
 180 about 0.3 Wm^{-2} smaller than F_a^m . When we compare the relative RMS errors (RMS error
 181 divided by the mean Aqua value) between radiance and flux, the relative flux RMS errors
 182 (6.4% for SW, 2.2% for daytime LW, and 1.4% for nighttime LW) are always slightly larger
 183 than the relative radiance RMS errors (6.0% for SW, 2.1% for daytime LW, and 1.1% for
 184 nighttime LW). This indicates that additional uncertainties are added when the radiances
 185 are converted to fluxes.

186 However, we cannot directly compare the gridded monthly mean fluxes from Aqua and
 187 NPP as their overpass times differ. Figure 3 shows the monthly mean TOA solar insolation
 188 difference between CERES-NPP and CERES-Aqua for April 2013. Solar insolation for NPP
 189 overpass times are greater than that for Aqua overpass times over most regions, except over
 190 the northern high latitude where NPP has significantly more overpasses at $\theta_0 > 70^\circ$ than
 191 Aqua. Regional differences as large as 30 Wm^{-2} are observed over the tropical regions and
 192 north of 60°N . Globally, the CERES-NPP monthly mean solar insolation is greater than
 193 that of CERES-Aqua by 13.4 Wm^{-2} for this month. When we compare the monthly gridded
 194 TOA reflected SW flux between CERES-NPP and CERES-Aqua, most of the features re-
 195 semble those of the insolation differences (not shown). We thus compare the albedo between
 196 CERES-NPP and CERES-Aqua (Figure 4). Over most regions, the albedo from CERES-
 197 NPP is greater than that from CERES-Aqua, except over parts of tropical oceans and

198 Antarctica where some negative differences are observed. The global monthly mean albedo
199 from CERES-NPP is greater than that from CERES-Aqua by 0.003 (1.02%). The albedo
200 difference is mostly from the calibration differences (see Figure 1a), while the footprint size
201 difference and scene identification difference also contribute to the albedo difference.

202 The CERES cloud working group developed sophisticated cloud detection algorithms
203 using visible and infrared channels of MODIS separately for polar and non-polar regions and
204 for daytime, twilight, and nighttime (Trepte et al. 2010). However, these detection algorithms
205 have to be modified to be applicable to the VIIRS observations (Qing Trepte, personal
206 communication), as some of the MODIS channels utilized for cloud detection are not available
207 on VIIRS. These modifications include replacing the 2.1 μm MODIS channel with the 1.6
208 μm VIIRS channel, and replacing detection tests using MODIS 6.7 μm and 13.3 μm channels
209 with VIIRS 3.7 μm and 11 μm channels, and supplement with tests utilizing VIIRS 1.6 μm
210 channel and the brightness temperature differences between 11 μm and 12 μm . These changes
211 mainly affect the cloud detections over the polar regions. The parameterization of 1.24
212 μm reflectance was regenerated for VIIRS using improved wavelength and solar insolation
213 weighting, which affects cloud optical depth retrieval over the snow/ice surfaces (Szedung
214 Sun-Mack, personal communication). These changes result in different cloud properties
215 retrieved using MODIS and VIIRS, especially over the polar regions. Figure 5 shows the
216 daytime cloud fraction and cloud optical depth difference between VIIRS and Aqua-MODIS
217 for April 2013. Cloud fraction retrieved from VIIRS is greater than that from MODIS by
218 up to 10% and cloud optical depth from VIIRS is smaller than that from MODIS by 2~3
219 over part of the Antarctic. Cloud fraction from VIIRS over the northern high-latitude snow
220 regions is smaller than that from MODIS, while the optical depth from VIIRS is greater
221 than that from MODIS. Over the Arctic, cloud optical depth from VIIRS is much larger
222 than that from MODIS. Over the ocean between 60°S and 60°N, the differences in cloud
223 fraction seem rather random while the differences in cloud optical depth is mostly positive
224 (VIIRS retrieval is greater than Aqua-MODIS retrieval).

225 Given that the footprint sizes and overpass times are different between CERES-Aqua
226 and CERES-NPP, in addition to the calibration differences and cloud retrieval differences
227 between them, fluxes from these CERES instruments cannot be compared directly to assess
228 the effects of footprint size difference and cloud property difference on flux uncertainty.

229 **3. Method**

230 To quantify the footprint size and cloud retrieval effect on flux inversion without having
231 to account for the calibration and overpass time differences, we design a simulation study
232 using the MODIS pixel level data and the Aqua-Earth-Sun geometry. MODIS spectral
233 measurements are used to retrieve cloud properties and aerosol optical depth. These pixel-
234 level imager-derived aerosol and cloud properties, and spectral narrowband (NB) radiances
235 from MODIS are convolved with the CERES PSF to provide the most accurate aerosol and
236 cloud properties that are spatially and temporally matched with the CERES broadband
237 radiance data. Figure 6 illustrates the process of generating the simulated CERES-Aqua
238 and CERES-NPP footprints from the MODIS pixels. We first use the CERES-Aqua PSF
239 to convolve the aerosol/cloud properties, and the MODIS NB radiances (and other ancillary
240 data) into Aqua-size footprints (left portion of Figure 6), as is done for the standard CERES-
241 Aqua SSF product. These NB radiances for the simulated CERES-Aqua footprints are
242 denoted as $I_a^s(\lambda)$, where superscript ‘s’ is for the simulated (in contrast to superscript ‘m’
243 for the measured). We then increase the footprint size to be that of NPP and use the
244 CERES-NPP PSF to average the MODIS NB radiances, cloud/aerosol properties, and other
245 ancillary data into the simulated NPP footprints. NB radiances for the simulated CERES-
246 NPP footprints are denoted as $I_n^s(\lambda)$.

247 Four months (July 2012, October 2012, January 2013, and April 2013) of simulated
248 CERES-Aqua and CERES-NPP data were created. For every CERES-Aqua footprint, it
249 contains the broadband SW and LW radiances measured by the CERES instrument. The

250 simulated NPP footprints, however, do not contain broadband radiances. To circumvent
251 this issue, we developed narrowband-to-broadband coefficients to convert the MODIS NB
252 radiances to broadband radiances.

253 The Edition 4 CERES-Aqua SSF data from July 2002 to September 2007 are used to
254 derive the narrowband-to-broadband (NB2BB) regression coefficients separately for SW,
255 daytime LW, and nighttime LW. Seven MODIS spectral bands (0.47, 0.55, 0.65, 0.86, 1.24,
256 2.13, and 3.7 μm) are used to derive the broadband SW radiances, and the SW regression
257 coefficients are calculated for every calendar month for discrete intervals of solar zenith angle,
258 viewing zenith angle, relative azimuth angle, surface type, snow/non-snow conditions, cloud
259 fraction, and cloud optical depth. Five MODIS spectral bands (6.7, 8.5, 11.0, 12.0, and 14.2
260 μm) are used to derive the broadband LW radiances, and the LW regression coefficients are
261 calculated for every calendar month for discrete intervals of viewing zenith angle, precipitable
262 water, surface type, snow/none-snow conditions, cloud fraction, and cloud optical depth. The
263 20 IGBP surface types are grouped into 8 surface types: ocean, forest, savanna, grassland,
264 dark desert, bright desert, the Greenland permanent snow, and the Antarctic permanent
265 snow. When there is sea ice over the ocean and snow over the land surface types, regression
266 coefficients for ice and snow conditions are developed (only footprints with 100% sea ice/snow
267 coverage are considered).

268 These SW and LW NB2BB regression coefficients are then applied to $I_a^s(\lambda)$ and $I_n^s(\lambda)$
269 to derive the broadband radiances, I_a^s and I_n^s , for simulated footprints of CERES-Aqua
270 and CERES-NPP, shown on the left and right of Figure 6, if the footprint consists of a
271 single surface type. As both simulated CERES-Aqua and CERES-NPP footprints use the
272 Aqua-Earth-Sun geometry, I_a^s and I_n^s have the same Sun-viewing geometry. Even though the
273 CERES-Aqua footprints contained the broadband radiances from CERES observations (I_a^m),
274 we choose to use the broadband radiances calculated using the NB2BB regressions to ensure
275 that I_a^s and I_n^s are consistently derived. Doing so we can isolate the flux differences between
276 simulated CERES-Aqua and simulated CERES-NPP caused by footprint size difference.

277 The cloud properties in the simulated CERES-Aqua footprints and in the simulated
278 CERES-NPP footprints are all based upon the MODIS retrievals, so the scene identifica-
279 tions used to select ADMs for flux inversion are almost the same for both the simulated
280 CERES-Aqua and the CERES-NPP, except for small differences due to differing footprint
281 sizes. As demonstrated in Figure 5, cloud properties differ between the MODIS and the VI-
282 IRS retrievals. These cloud retrieval differences affect the anisotropy factors selected for flux
283 inversion. To simulate both the footprint size and cloud property differences, cloud fraction
284 and cloud optical depth retrievals from MODIS convolved in the simulated CERES-NPP
285 footprints are adjusted to be similar to those from VIIRS retrievals to assess how cloud
286 retrieval differences affect the flux. To accomplish this, daily cloud fraction ratios of VIIRS
287 to MODIS are calculated for each 1° latitude by 1° longitude grid box. These ratios are then
288 applied to the cloudy footprints of MODIS retrieval to adjust the MODIS cloud fractions
289 to be nearly the same as those from VIIRS retrieval. Note no adjustment is done for clear
290 footprints. Similarly, daily cloud optical depth ratios of VIIRS to MODIS are calculated us-
291 ing cloudy footprints for each 1° by 1° grid box. These ratios are used to adjust the MODIS
292 retrieved cloud optical depth to be close to those from VIIRS retrievals. The process of gen-
293 erating the simulated CERES-NPP footprints with VIIRS-like cloud retrievals is illustrated
294 on the lower right portion of Figure 6.

295 Aqua ADMs are then used to convert I_a^s and I_n^s to fluxes, F_a^s and F_n^s , for the simulated
296 CERES-Aqua and CERES-NPP footprints using the cloud properties retrieved from MODIS
297 observations for scene type identification. To further access the effects of both footprint size
298 and cloud property differences on flux inversion, Aqua ADMs are used to convert I_n^s to flux,
299 $F_n'^s$, for the simulated CERES-NPP footprints using VIIRS-like cloud properties for scene
300 identification.

4. Results

We first compare the footprint-level fluxes between simulated CERES-Aqua and simulated CERES-NPP using data of April 1, 2013 (about 700,000 footprints). As the cloud fraction and cloud optical depth adjustments are done at the grid box level, it is not feasible to compare footprint-level $F'_n{}^s$ and $F'_n{}^s$, and only footprint-level $F_a{}^s$ and $F_n{}^s$ are compared. For SW, the bias between $F_a{}^s$ and $F_n{}^s$ is 0.1 Wm^{-2} and the RMS error is 4.7 Wm^{-2} . For LW, the biases is close to zero and the RMS errors are 1.3 Wm^{-2} and 0.9 Wm^{-2} for daytime and nighttime, respectively. These flux RMS errors are much smaller than those listed in Table 1, indicating that calibration differences are responsible for most of the flux differences between CERES-Aqua and CERES-NPP measurements. However, we should avoid direct comparisons between these two sets of RMS errors, as they are derived using different time period.

We now compare the monthly grid box (1° latitude by 1° longitude) mean fluxes from the three simulations outlined in the previous section. Differences between $F'_n{}^s$ and $F_a{}^s$ are used to assess the CERES-NPP gridded monthly mean instantaneous flux uncertainties due to the footprint size difference, and differences between $F'_n{}^s$ and $F_a{}^s$ are used to assess the CERES-NPP gridded monthly mean instantaneous flux uncertainties due to both the footprint size and cloud property differences.

The monthly mean instantaneous TOA SW fluxes for simulated CERES-Aqua ($F_a{}^s$) are shown in Figure 7(a) for April 2013. Note these fluxes are different from those in the Edition 4 Aqua SSF product as the CERES measured radiances differ from those inferred using NB2BB regression coefficients. The flux differences caused by the footprint size difference between the simulated CERES-NPP and the simulated CERES-Aqua ($F'_n{}^s - F_a{}^s$) are shown in Figure 7(b). Grid boxes in white indicate that the number of footprints with valid SW fluxes differ by more than 2% between simulated CERES-Aqua and CERES-NPP, as the NB2BB regressions are only applied to footprints that are consist of the same surface types which result in fewer footprints with valid fluxes for CERES-NPP than for CERES-Aqua. The

328 footprint size difference between CERES-Aqua and CERES-NPP introduces an uncertainty
329 that rarely exceeds 4.0 Wm^{-2} in monthly gridded CERES-NPP instantaneous SW fluxes.
330 For global monthly mean instantaneous SW flux, the simulated CERES-NPP has a low bias
331 of 0.4 Wm^{-2} compares to the simulated CERES-Aqua, and the RMS error between them is
332 2.4 Wm^{-2} . Results from the other three months are very similar to April 2013 (not shown).

333 Figure 7(c) shows the SW flux difference caused by both the footprint size and cloud prop-
334 erty differences ($F_n'^s - F_a^s$). Adding the cloud property differences increase the CERES-NPP
335 flux uncertainty comparing to when only footprint size differences are considered (Figure
336 7(b)), monthly gridded instantaneous flux uncertainty over the Arctic ocean can exceed 20
337 Wm^{-2} . Accounting for cloud property differences, the global monthly mean instantaneous
338 SW flux from simulated CERES-NPP has a high bias of 1.1 Wm^{-2} and the RMS error is
339 increased to 5.2 Wm^{-2} . Over the Arctic Ocean, the cloud optical depth from VIIRS retrieval
340 is much greater than that from the MODIS retrieval while the difference in cloud fraction is
341 relatively small. Anisotropic factors for thick clouds are smaller than those for thin clouds
342 at oblique viewing angles, and are larger for near-nadir viewing angles. The viewing ge-
343 ometries over the Arctic Ocean produced more smaller anisotropic factors than larger ones
344 when MODIS cloud optical depths were replaced with VIIRS-like cloud optical depths, which
345 resulted in larger fluxes when using VIIRS-like cloud properties for flux inversion.

346 The daytime and nighttime LW flux from the simulated CERES-Aqua footprints, LW
347 flux differences due to footprint size difference, and LW flux difference due to both footprint
348 size difference and cloud property difference are shown in Figures 8 and 9. The effect of
349 footprint size on gridded monthly mean daytime and nighttime LW flux is generally within
350 1.0 Wm^{-2} . For global monthly mean LW flux, the differences between $F_n^s - F_a^s$ are close to
351 zero, and the RMS errors between them are about 0.8 Wm^{-2} and 0.2 Wm^{-2} for daytime
352 and nighttime LW fluxes. When cloud property differences are also considered, their effect
353 on gridded monthly mean LW fluxes increases to about 2 Wm^{-2} . The RMS errors of global
354 monthly mean LW flux increase slightly to about 0.9 Wm^{-2} and 0.5 Wm^{-2} for daytime and

355 nighttime. The LW fluxes showed much less sensitivity to cloud property changes than the
356 SW fluxes, especially over the Arctic Ocean where cloud optical depth changed significantly.
357 This is because the LW ADMs over the snow/ice surfaces have very little sensitivity to cloud
358 optical depth (Su et al. 2015a), but they were developed for discrete cloud fraction intervals
359 and larger flux changes are noted in regions experiencing large cloud fraction changes.

360 5. Summary and discussion

361 The scene-type dependent ADMs are used to convert the radiances measured by the
362 CERES instruments to fluxes. Specific empirical ADMs were developed for CERES instru-
363 ments on TRMM, Terra, and Aqua (Loeb et al. 2003, 2005; Su et al. 2015a). As there is only
364 one CERES instrument on NPP and it has been placed in cross-track mode since launch,
365 it is not possible to construct a set of ADMs specific for CERES on NPP. Edition 4 Aqua
366 ADMs (Su et al. 2015a) are thus used for flux inversions for CERES-NPP measurements.
367 However, the altitude of the NPP orbit is higher than that of the Aqua orbit resulting in
368 a larger CERES footprint size on NPP than on Aqua. Given that the footprint size of
369 CERES-NPP is different from that of CERES-Aqua, we need to quantify the CERES-NPP
370 flux uncertainty caused by using the CERES-Aqua ADMs. Furthermore, there are some
371 differences between the imagers that are on the same spacecrafts as CERES-Aqua (MODIS)
372 and CERES-NPP (VIIRS), as VIIRS lacks the $6.7 \mu\text{m}$ and $13.3 \mu\text{m}$ channels. These spectral
373 differences and algorithm differences lead to notable cloud fraction and cloud optical depth
374 differences retrieved from MODIS and VIIRS. As the anisotropy factors are scene-type de-
375 pendent, differences in cloud properties will also introduce uncertainties in flux inversion.
376 Furthermore, the calibrations between CERES instruments on Aqua and on NPP also are
377 different from each other. Comparisons using two years of collocated CERES-Aqua and
378 CERES-NPP footprints indicate that the SW radiances from CERES-NPP are about 1.5%
379 greater than those from CERES-Aqua, the daytime LW radiances from CERES-NPP are

380 about 0.5% smaller than those from CERES-Aqua, and the nighttime LW radiances agree
381 to within 0.1%.

382 To quantify the flux uncertainties due to the footprint size difference between CERES-
383 Aqua and CERES-NPP, and due to both the footprint size difference and cloud property
384 difference, we use the MODIS pixel level data to simulate the CERES-Aqua and CERES-
385 NPP footprints. The simulation is designed to isolate the effects of footprint size differ-
386 ence and cloud property difference on flux uncertainty from calibration difference between
387 CERES-NPP and CERES-Aqua. The pixel-level MODIS spectral radiances, the imager-
388 derived aerosol and cloud properties, and other ancillary data are first convolved with the
389 CERES Aqua PSF to generate the simulated CERES-Aqua footprints, and then convolved
390 with the CERES NPP PSF to generate the simulated CERES-NPP footprints. Broadband
391 radiances within the simulated CERES-Aqua and CERES-NPP footprints are derived us-
392 ing the MODIS spectral bands based upon narrowband-to-broadband regression coefficients
393 developed using five years of Aqua data to ensure consistency between broadband radi-
394 ances from simulated CERES-Aqua and CERES-NPP. These radiances are then converted
395 to fluxes using the CERES-Aqua ADMs. The footprint size difference between CERES-Aqua
396 and CERES-NPP introduces instantaneous flux uncertainties in monthly gridded CERES-
397 NPP of less than 4.0 Wm^{-2} for SW, and less than 1.0 Wm^{-2} for both daytime and nighttime
398 LW. The global monthly mean instantaneous SW flux from simulated CERES-NPP has a
399 low bias of 0.4 Wm^{-2} compares to that from simulated CERES-Aqua, and the RMS error
400 between them is 2.4 Wm^{-2} . The biases in global monthly mean LW fluxes are close to zero,
401 and the RMS errors between simulated CERES-NPP and simulated CERES-Aqua are about
402 0.8 Wm^{-2} and 0.2 Wm^{-2} for daytime and nighttime global monthly mean LW fluxes.

403 The cloud properties in the simulated CERES-Aqua footprints and in the simulated
404 CERES-NPP footprints are all based upon MODIS retrievals, but in reality cloud prop-
405 erties retrieved from VIIRS differ from those from MODIS. To assess the flux uncertainty
406 from scene identification differences, cloud fraction and cloud optical depth in the simulated

407 CERES-NPP footprints are perturbed to be more like the VIIRS retrievals. When both
408 footprint size and cloud property differences are considered, the uncertainties of monthly
409 gridded CERES-NPP SW flux can be up to 20 Wm^{-2} in the Arctic regions where cloud
410 optical depth retrievals from VIIRS differ significantly from MODIS. The global monthly
411 mean instantaneous SW flux from simulated CERES-NPP has a high bias of 1.1 Wm^{-2} and
412 the RMS error is increased to 5.2 Wm^{-2} . LW flux shows less sensitivity to cloud property
413 differences than SW flux, with the uncertainties of about 2.0 Wm^{-2} in monthly gridded LW
414 flux, and the RMS errors increases to 0.9 Wm^{-2} and 0.5 Wm^{-2} for daytime and nighttime
415 LW flux.

416 Su et al. (2015b) quantified the global monthly 24hr-averaged flux uncertainties due to
417 CERES ADMs using direct integration tests, and concluded that the RMS errors are less
418 than 1.1 Wm^{-2} and 0.8 Wm^{-2} for 24hr-averaged TOA SW and LW fluxes. The uncertainty
419 for global monthly instantaneous SW flux is approximately twice the uncertainty of 24hr-
420 averaged flux. This simulation study indicates that the footprint size differences between
421 CERES-NPP and CERES-Aqua introduce flux uncertainties that are within the uncertain-
422 ties of the CERES ADMs. However, the uncertainty assessment provided here should be
423 considered as the low end, as many regions (especially over land, snow, and ice) were not
424 included due to sample number differences within the grid boxes. When cloud property
425 differences are accounted for, the SW flux uncertainties increase significantly and exceed the
426 uncertainties of the CERES ADMs. These findings indicate that inverting CERES-NPP flux
427 using CERES-Aqua ADMs resulting in flux uncertainties that are within the ADMs uncer-
428 tainties as long as the cloud retrievals between VIIRS and MODIS are consistent. When
429 the cloud retrieval differences between VIIRS and MODIS are accounted for, the SW flux
430 uncertainties exceed those of the CERES ADMs. To maintain the consistency of the CERES
431 climate data record, it is thus important to develop cloud retrieval algorithms that account
432 for the capabilities of both MODIS and VIIRS to ensure consistent cloud properties from
433 both imagers.

435 *Acknowledgments.*

436 This research was supported by the NASA CERES project. The CERES data were ob-
437 tained from the NASA Langley Atmospheric Science Data Center at [https://eosweb.larc.nasa.](https://eosweb.larc.nasa.gov/project/ceres/ssf_table)
438 [gov/project/ceres/ssf_table](https://eosweb.larc.nasa.gov/project/ceres/ssf_table). We thank Norman Loeb, Szedung Sun-Mack, Qing Treppe, and
439 Patrick Minnis for helpful discussions, and the three reviewers for their constructive com-
440 ments and suggestions which have significantly improved this paper.

REFERENCES

- 443 Di Girolamo, L., T. Varnai, and R. Davies, 1998: Apparent breakdown of reciprocity in
444 reflected solar radiances. *J. Geophys. Res.*, **103 (D8)**, 8795–8803.
- 445 Kato, S., et al., 2011: Improvements of top-of-atmosphere and surface irradiance computa-
446 tion with CALIPSO-, and MODIS-derived cloud and aerosol properties. *J. Geophys. Res.*,
447 **116 (D19209)**, D19 209, doi:10.1029/2011JD016050.
- 448 Loeb, N. G., S. Kato, K. Loukachine, and N. Manalo-Smith, 2005: Angular distribution
449 models for top-of-atmosphere radiative flux estimation from the clouds and the earth’s
450 radiant energy system instrument on the terra satellite. part I: Methodology. *J. Atmos.*
451 *Oceanic Technol.*, **22**, 338–351.
- 452 Loeb, N. G., J. M. Lyman, G. C. Johnson, R. P. Allan, D. R. Doelling, T. Wong, B. J.
453 Soden, and G. L. Stephens, 2012: Observed changes in top-of-the-atmosphere radiation
454 and upper-ocean heating consistent within uncertainty. *Nature Geosci.*, **5**, 110–113, doi:
455 10.1038/NGEO1375.
- 456 Loeb, N. G. and N. Manalo-Smith, 2005: Top-of-atmosphere direct radiative effect of aerosols
457 over global oceans from merged CERES and MODIS observations. *J. Climate*, **18**, 3506–
458 3526.
- 459 Loeb, N. G., N. Manalo-Smith, S. Kato, W. F. Miller, S. K. Gupta, P. Minnis, and B. A.
460 Wielicki, 2003: Angular distribution models for top-of-atmosphere radiative flux estima-
461 tion from the Clouds and the Earth’s Radiant Energy System instrument on the Tropical
462 Rainfall Measuring Mission satellite. Part I: Methodology. *J. Appl. Meteor.*, **42**, 240–265.

- 463 Loeb, N. G., N. Manalo-Smith, W. Su, M. Shankar, and S. Thomas, 2016: CERES top-of-
464 atmosphere Earth radiation budget climate data record: Accounting for in-orbit changes
465 in instrument calibration. *Remote Sens.*, **8 (182)**, doi:10.3390/rs8030182.
- 466 Loeb, N. G. and G. L. Schuster, 2008: An observational study of the relationship between
467 cloud, aerosol and meteorology in broken low-level cloud conditions. *J. Geophys. Res.*,
468 **113 (D14214)**, D14 214, doi:10.1029/2007JD009763.
- 469 Loveland, T. R. and A. S. Belward, 1997: The international geosphere biosphere programme
470 data and information system global land cover dataset (DISCover). *Acta Astronaut.*, **41**,
471 681–689.
- 472 Minnis, P., et al., 2010: CERES Edition 3 cloud retrievals. *13th Conference on Atmospheric*
473 *Radiation*, Am. Meteorol. Soc., Oregon, Portland.
- 474 Pincus, R., C. P. Batstone, R. J. P. Hofmann, K. E. Taylor, and P. J. Glecker, 2008: Evalu-
475 ating the present-day simulation of clouds, precipitation, and radiation in climate models.
476 *J. Geophys. Res.*, **113 (D14209)**, D14 209, doi:10.1029/2007JD009334.
- 477 Quaas, J., O. Boucher, N. Bellouin, and S. Kinne, 2008: Satellite-based estimate of the
478 direct and indirect aerosol climate forcing. *J. Geophys. Res.*, **113 (D05204)**, D05 204,
479 doi:10.1029/2007JD008962.
- 480 Satheesh, S. K. and V. Ramanathan, 2000: Large differences in tropical aerosol forcing at
481 the top of the atmosphere and earth’s surface. *Nature*, **405**, 60–63.
- 482 Smith, G. L., 1994: Effects of time response on the point spread function of a scanning
483 radiometer. *Appl. Opt.*, **33**, 7031–7037.
- 484 Stephens, G. L., et al., 2012: An update on Earth’s energy balance in light of the latest
485 global observations. *Nature Geosci.*, **5**, 691–696, doi:10:1038/NGEO1580.

486 Su, W., A. Bodas-Salcedo, K.-M. Xu, and T. P. Charlock, 2010a: Comparison of the trop-
487 ical radiative flux and cloud radiative effect profiles in a climate model with Clouds and
488 the Earth’s Radiant Energy System (CERES) data. *J. Geophys. Res.*, **115** (D01105),
489 D01 105, doi:10.1029/2009JD012490.

490 Su, W., J. Corbett, Z. A. Eitzen, and L. Liang, 2015a: Next-generation angular distribution
491 models for top-of-atmosphere radiative flux calculation from the CERES instruments:
492 Methodology. *Atmos. Meas. Tech.*, **8**, 611–632, doi:10.5194/amt-8-611-2015.

493 Su, W., J. Corbett, Z. A. Eitzen, and L. Liang, 2015b: Next-generation angular distribution
494 models for top-of-atmosphere radiative flux calculation from the CERES instruments:
495 Validation. *Atmos. Meas. Tech.*, **8**, 3297–3313, doi:10.5194/amt-8-3297-2015.

496 Su, W., N. G. Loeb, G. L. Schuster, M. Chin, and F. G. Rose, 2013: Global all-sky shortwave
497 direct radiative forcing of anthropogenic aerosols from combined satellite observations and
498 GOCART simulations. *J. Geophys. Res.*, **118**, 1–15, doi:10.1029/2012JD018294.

499 Su, W., N. G. Loeb, K. Xu, G. L. Schuster, and Z. A. Eitzen, 2010b: An estimate of aerosol
500 indirect effect from satellite measurements with concurrent meteorological analysis. *J.*
501 *Geophys. Res.*, **115** (D18219), D18 219, doi:10.1029/2010JD013948.

502 Trenberth, K. E., J. T. Fasullo, and J. Kiehl, 2009: Earth’s global energy budget. *Bull. Am.*
503 *Meteor. Soc.*, **90**, 311–323, doi:10.1175/2008BAMS2634.1.

504 Trepte, Q. Z., P. Minnis, C. Trepte, and S. Sun-Mack, 2010: Improved cloud detections in
505 CERES Edition 3 algorithm and comparison with the CALIPSO vertical feature mask.
506 *13th Conference on Atmospheric Radiation*, Am. Meteorol. Soc., Oregon, Portland.

507 Wang, H. and W. Su, 2013: Evaluating and understanding top of the atmosphere cloud
508 radiative effects in Intergovernmental Panel on Climate Change (IPCC) fifth assessment
509 report (AR5) coupled model intercomparison project phase 5 (CMIP5) models using
510 satellite observations. *J. Geophys. Res.*, **118**, 1–17, doi:10.1029/2012JD018619.

- 511 Wielicki, B. A., B. R. Barkstrom, E. F. Harrison, R. B. Lee, G. L. Smith, and J. E. Cooper,
512 1996: Clouds and the Earth's Radiant Energy System (CERES): An Earth Observing
513 System experiment. *Bull. Amer. Meteor. Soc.*, **77**, 853–868.
- 514 Wild, M., D. Folini, C. Schar, N. G. Loeb, E. G. Dutton, and G. Konig-Langlo, 2013:
515 The global energy balance from a surface perspective. *Clim. Dyn.*, **40**, 3107–3134, doi:
516 10.1007/s00382-012-1569-8.
- 517 Zhang, J., S. A. Christopher, L. A. Remer, and Y. J. Kaufman, 2005: Shortwave aerosol
518 radiative forcing over cloud-free oceans from Terra: 2. Seasonal and global distributions.
519 *J. Geophys. Res.*, **110 (D10S24)**, D10S24, doi:10.1029/2004JD005009.

520 **List of Tables**

521 1 Comparison of CERES-Aqua and CERES-NPP measured SW, daytime LW,
522 and nighttime LW radiances ($\text{Wm}^{-2}\text{sr}^{-1}$) and fluxes (Wm^{-2}) using matched
523 footprints of 2013 and 2014. 24

TABLE 1. Comparison of CERES-Aqua and CERES-NPP measured SW, daytime LW, and nighttime LW radiances ($\text{Wm}^{-2}\text{sr}^{-1}$) and fluxes (Wm^{-2}) using matched footprints of 2013 and 2014.

	SW	Daytime LW	Nighttime LW
Sample Number	147894	192178	187880
Mean CERES-Aqua Radiance	68.1	77.4	74.4
Mean CERES-NPP Radiance	69.2	77.0	74.3
Radiance RMS Error	4.1	1.6	0.8
Mean CERES-Aqua Flux	230.1	235.7	226.4
Mean CERES-NPP Flux	233.9	234.7	226.1
Flux RMS Error	14.6	5.0	3.1

524 List of Figures

- 525 1 Radiance comparisons between matched CERES-Aqua and CERES-NPP foot-
526 prints, (a) SW; (b) daytime LW; and (c) nighttime LW using data of 2013
527 and 2014. 27
- 528 2 Flux comparisons between matched CERES-Aqua and CERES-NPP foot-
529 prints, (a) SW; (b) daytime LW; and (c) nighttime LW using data of 2013
530 and 2014. 28
- 531 3 Monthly mean solar insolation difference (Wm^{-2}) between CERES-NPP and
532 CERES-Aqua (NPP-Aqua) for April 2013. 29
- 533 4 Monthly mean albedo difference between CERES-NPP and CERES-Aqua
534 (NPP-Aqua) for April 2013. 30
- 535 5 Cloud fraction (a) and cloud optical depth (b) differences between VIIRS and
536 MODIS (VIIRS-MODIS) retrievals for April 2013. 31
- 537 6 Schematic diagram of convoluting the MODIS pixels into the simulated Aqua
538 and NPP footprints. Left depicts the processes involved in producing the
539 simulated Aqua footprints; middle for simulated NPP footprints with MODIS
540 retrievals; and right for simulated NPP footprints with VIIRS-like retrievals. 32
- 541 7 The gridded monthly mean TOA instantaneous SW fluxes from the simulated
542 Aqua footprints (F_a^s , a), the flux differences caused by footprint size difference
543 between simulated NPP and simulated Aqua ($F_n^s - F_a^s$, b), and the flux differ-
544 ences caused by both footprint size and cloud property differences ($F_n'^s - F_a^s$,
545 c) using April 2013 data. Regions shown in white have large sample number
546 differences between simulated Aqua and simulated NPP. 33

- 547 8 The gridded monthly mean TOA daytime LW fluxes from the simulated Aqua
548 footprints (F_a^s , a), the flux differences caused by footprint size difference be-
549 tween simulated NPP and simulated Aqua ($F_n^s - F_a^s$, b), and the flux differ-
550 ences caused by both footprint size and cloud property differences ($F_n'^s - F_a^s$,
551 c) using April 2013 data. Regions shown in white have large sample number
552 differences between simulated Aqua and simulated NPP. 34
- 553 9 The gridded monthly mean TOA nighttime LW fluxes from the simulated
554 Aqua footprints (F_a^s , a), the flux differences caused by footprint size difference
555 between simulated NPP and simulated Aqua ($F_n^s - F_a^s$, b), and the flux differ-
556 ences caused by both footprint size and cloud property differences ($F_n'^s - F_a^s$,
557 c) using April 2013 data. Regions shown in white have large sample number
558 differences between simulated Aqua and simulated NPP. 35

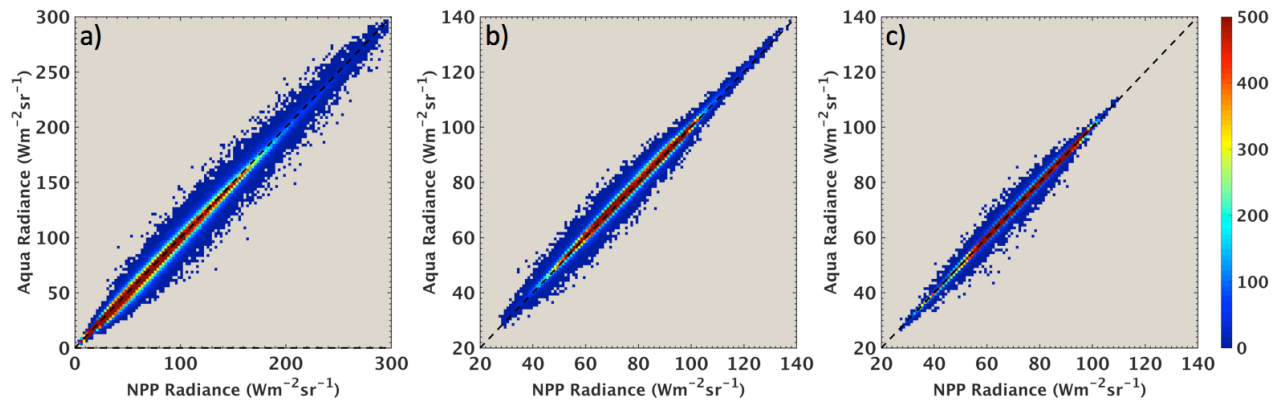


FIG. 1. Radiance comparisons between matched CERES-Aqua and CERES-NPP footprints, (a) SW; (b) daytime LW; and (c) nighttime LW using data of 2013 and 2014.

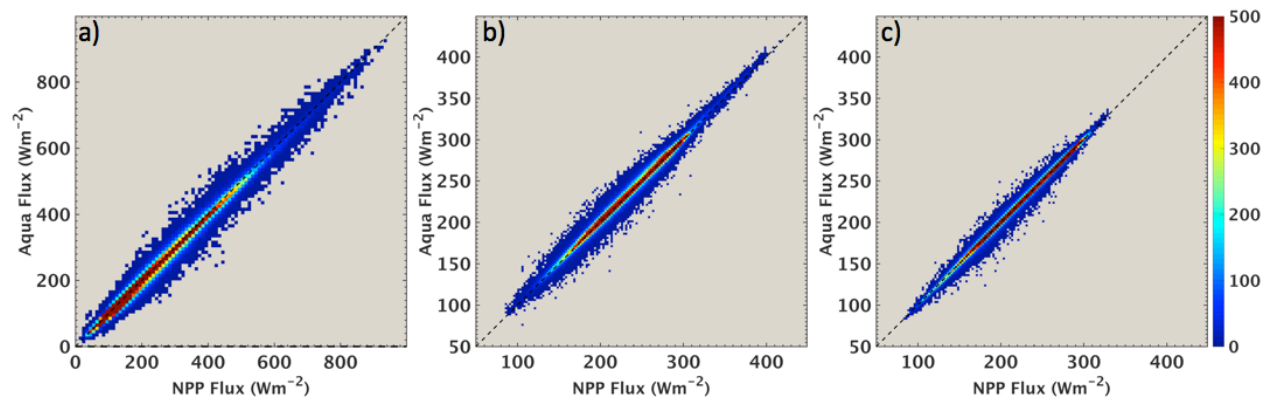


FIG. 2. Flux comparisons between matched CERES-Aqua and CERES-NPP footprints, (a) SW; (b) daytime LW; and (c) nighttime LW using data of 2013 and 2014.

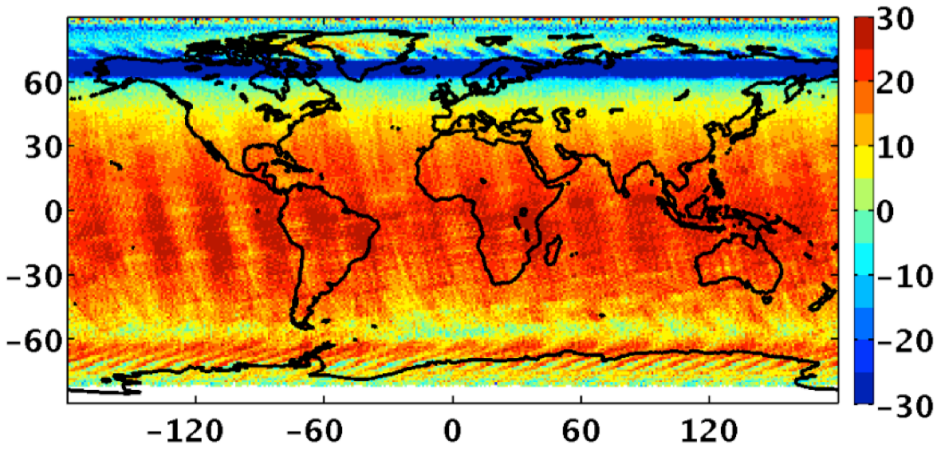


FIG. 3. Monthly mean solar insolation difference (Wm^{-2}) between CERES-NPP and CERES-Aqua (NPP-Aqua) for April 2013.

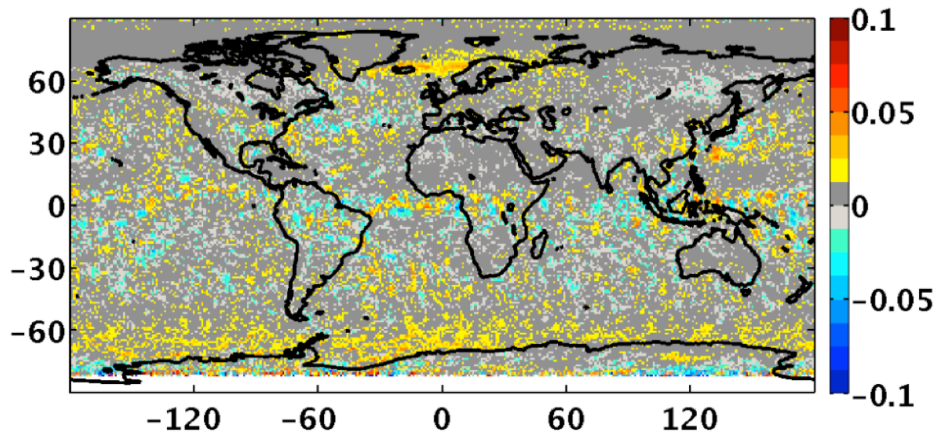


FIG. 4. Monthly mean albedo difference between CERES-NPP and CERES-Aqua (NPP-Aqua) for April 2013.

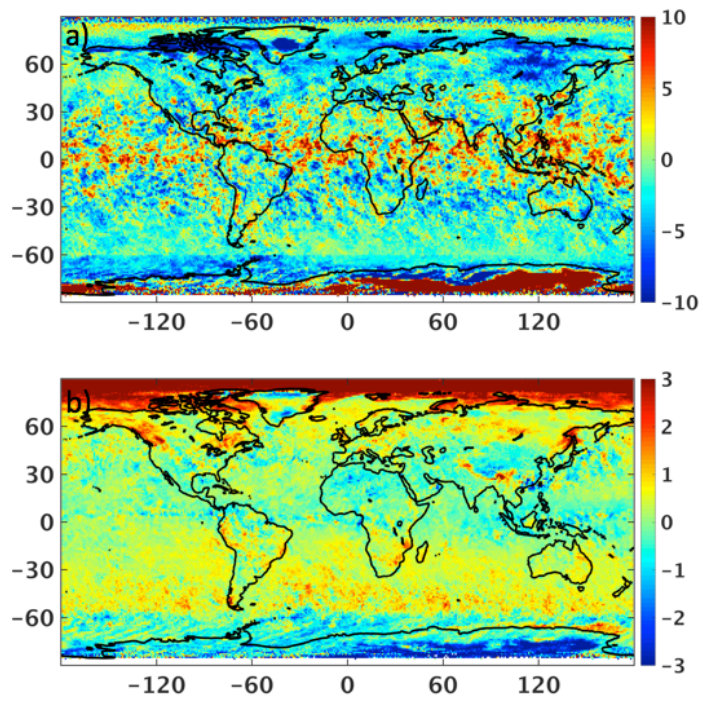


FIG. 5. Cloud fraction (a) and cloud optical depth (b) differences between VIIRS and MODIS (VIIRS-MODIS) retrievals for April 2013.

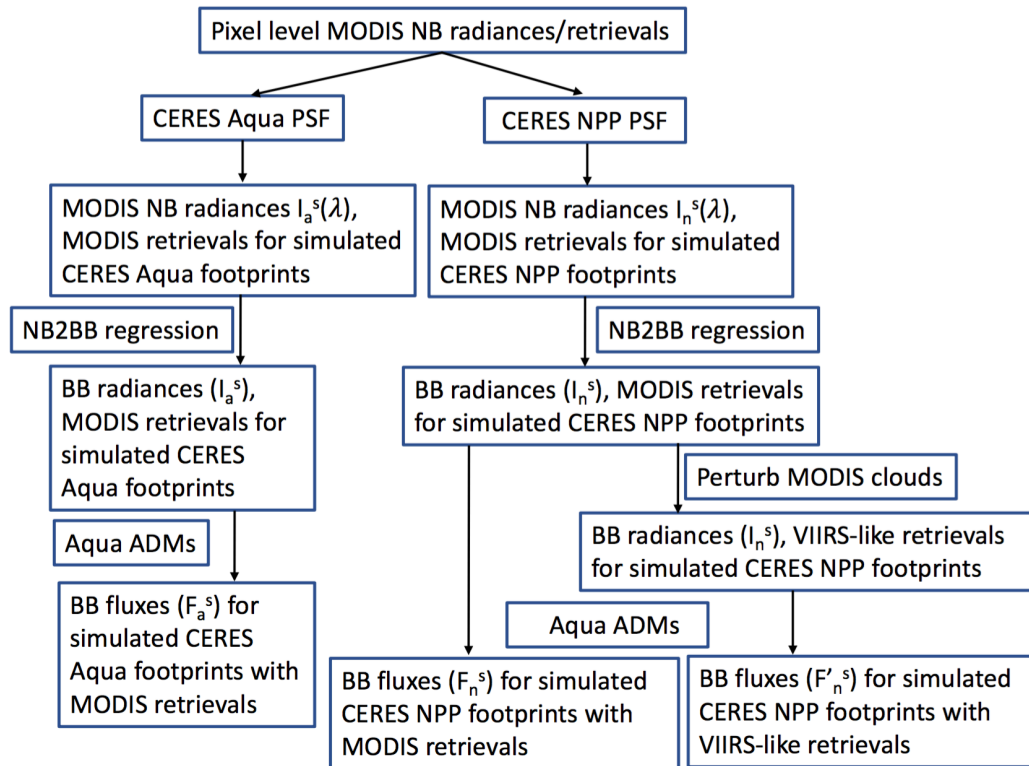


FIG. 6. Schematic diagram of convoluting the MODIS pixels into the simulated Aqua and NPP footprints. Left depicts the processes involved in producing the simulated Aqua footprints; middle for simulated NPP footprints with MODIS retrievals; and right for simulated NPP footprints with VIIRS-like retrievals.

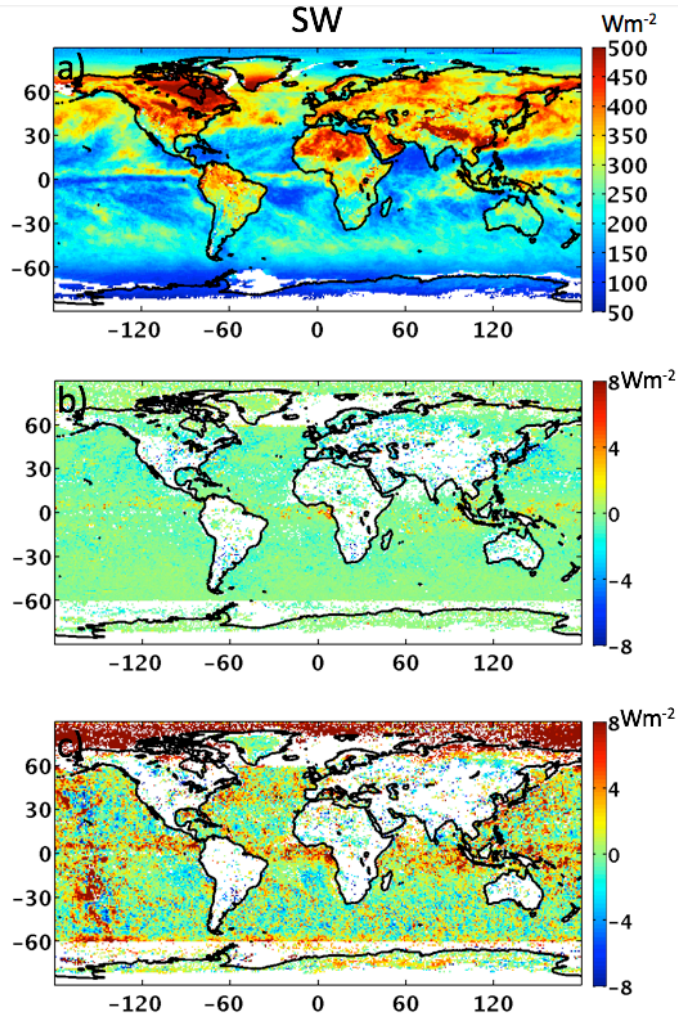


FIG. 7. The gridded monthly mean TOA instantaneous SW fluxes from the simulated Aqua footprints (F_a^s , a), the flux differences caused by footprint size difference between simulated NPP and simulated Aqua ($F_n^s - F_a^s$, b), and the flux differences caused by both footprint size and cloud property differences ($F_n'^s - F_a^s$, c) using April 2013 data. Regions shown in white have large sample number differences between simulated Aqua and simulated NPP.

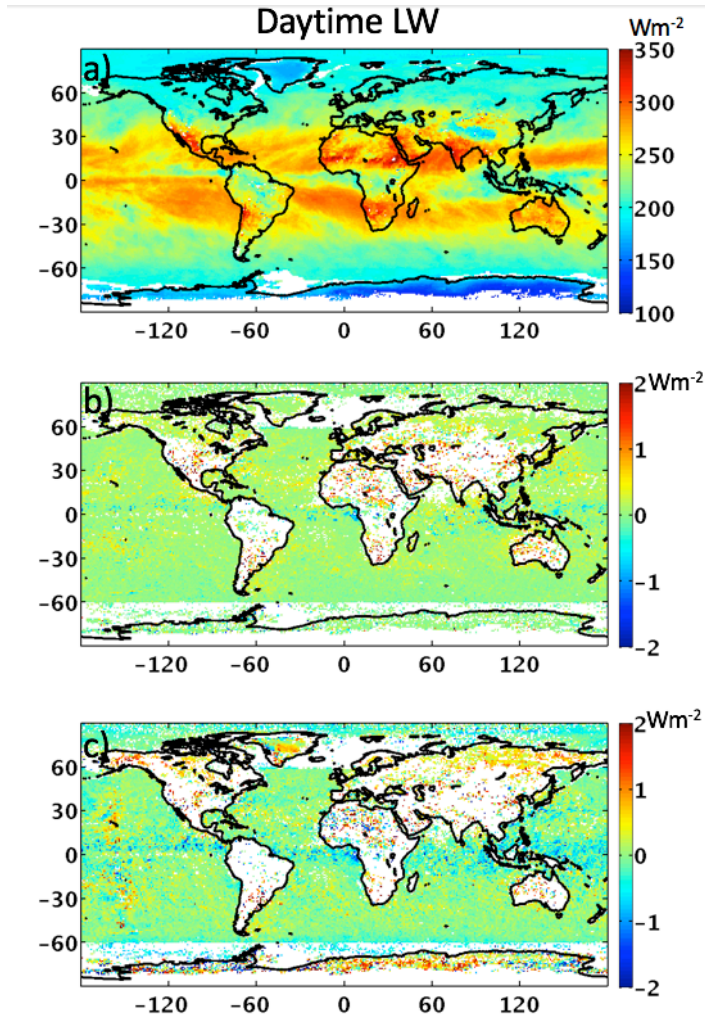


FIG. 8. The gridded monthly mean TOA daytime LW fluxes from the simulated Aqua footprints (F_a^s , a), the flux differences caused by footprint size difference between simulated NPP and simulated Aqua ($F_n^s - F_a^s$, b), and the flux differences caused by both footprint size and cloud property differences ($F_n'^s - F_a^s$, c) using April 2013 data. Regions shown in white have large sample number differences between simulated Aqua and simulated NPP.

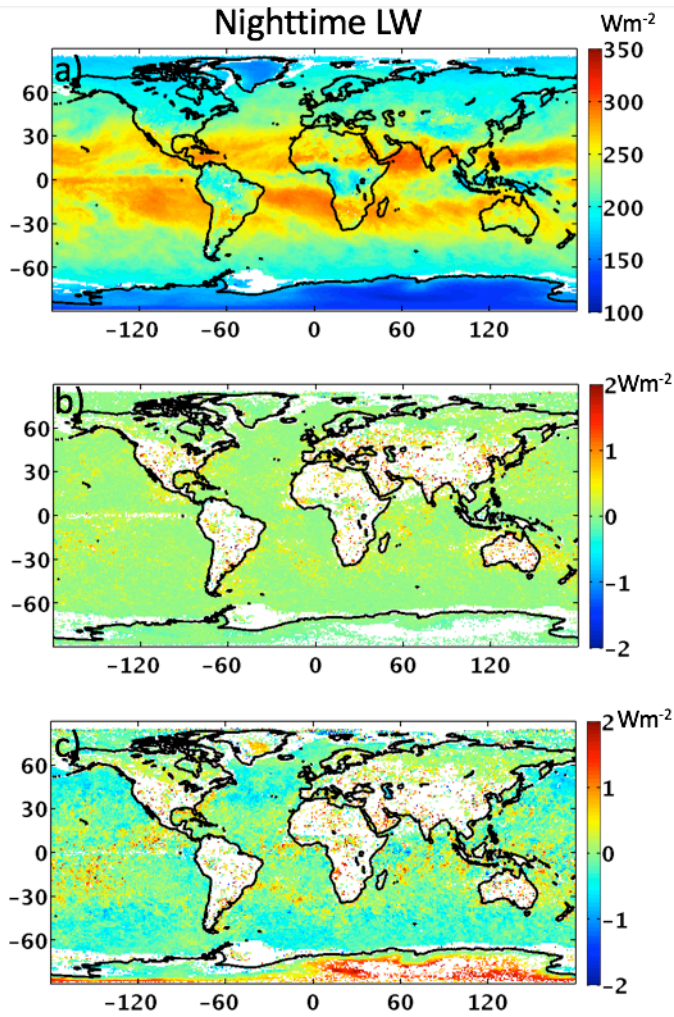


FIG. 9. The gridded monthly mean TOA nighttime LW fluxes from the simulated Aqua footprints (F_a^s , a), the flux differences caused by footprint size difference between simulated NPP and simulated Aqua ($F_n^s - F_a^s$, b), and the flux differences caused by both footprint size and cloud property differences ($F_n'^s - F_a^s$, c) using April 2013 data. Regions shown in white have large sample number differences between simulated Aqua and simulated NPP.